Nanoscale

PAPER

View Article Online
View Journal | View Issue

Cite this: *Nanoscale*, 2023, **15**, 13297

Anisotropy and thermal properties in GeTe semiconductor by Raman analysis†

Shuai Yang, Fengrui Sui, Yucheng Liu, Ruijuan Qi,* Xiaoyu Feng, Shangwei Dong, Pingxiong Yang and Fangyu Yue*

Received 7th June 2023,
Accepted 24th July 2023

DOI: 10.1039/d3nr02678g

rsc.li/nanoscale

Low-symmetric GeTe semiconductors have attracted wide-ranging attention due to their excellent optical and thermal properties, but only a few research studies are available on their in-plane optical anisotropic nature that is crucial for their applications in optoelectronic and thermoelectric devices. Here, we investigate the optical interactions of anisotropy in GeTe using polarization-resolved Raman spectroscopy and first-principles calculations. After determining both armchair and zigzag directions in GeTe crystals by transmission electron microscopy, we found that the Raman intensity of the two main vibrational modes had a strong in-plane anisotropic nature; the one at ~88.1 cm^{-1} can be used to determine the crystal orientation, and the other at ~124.6 cm^{-1} can reveal a series of temperature-dependent phase transitions. These results provide a general approach for the investigation of the anisotropy of light–matter interactions in low-symmetric layered materials, benefiting the design and application of optoelectronic, anisotropic thermoelectric, and phase-transition memory devices based on bulk GeTe.

1. Introduction

Low-symmetric two-dimensional (2D) layered materials present intriguing in-plane anisotropy.[1–4] For instance, GaTe, GeSe, GeAs, and black phosphorus have been reported to have significant directional dependence of their photoemission, thermoelectricity, and mobility properties, mainly due to the anisotropic light–matter interactions, such as the electron–photon and electron–phonon couplings.[1,2,4–8] As a typical binary IV–VI chalcogenide with a rhombohedral (α-phase; or pseudo-cubic) crystal structure at room temperature that is formed by distortion at high-temperature of the cubic phase,[9,10] GeTe ($R3m$-C_{3v} space group) has advantages for application in thermal-/opto-electronic devices, *e.g.*, with a maximum thermoelectric figure-of-merit (ZT) value of ~0.8 that can be improved up to the currently known 2.7 at 750 K (ref. 11) by elemental doping, as well as substitution or alloying with other compounds.[12–16] Based on the successful realization of the electrical control of the electronic spin states, GeTe can be used to prepare spin and photovoltaic devices due to its giant bulk Rashba spin–orbit coupling,[17–19] strong ferroelectric polarization (64–70 μC cm^{-2}), and high ferroelectric transition temperature.[20,21] Simultaneously, GeTe has been widely used in phase-change memory devices and phase-change switches because of its reversible phase change (*e.g.*, α and β phases), rapid crystallization, and a great difference among the optical and electrical properties of amorphous and crystalline states.[22–27] More importantly, as a member of the family of low-symmetric layered materials, GeTe has a narrow bandgap (E_g) of ~0.7 eV, which is rather useful for infrared optoelectronic devices, including light-emission and light-detection.[28,29] For example, Zhao *et al.* reported a prototype photodetector based on GeTe films with a high responsivity of 10^2 A W^{-1} and a detectivity of 10^{13} Jones under irradiation with an 850 nm laser.[30] These suggest that, being a low-symmetric laminate material with strong anisotropic nature, GeTe has the potential to be a promising material for use in polarization-dependent optothermal or optoelectrical devices. However, only a few studies have focused on its in-plane anisotropy and no unified consensus is found on the study of its vibrational modes and the phase transition relationships.

In this work, we investigate the in-plane anisotropy of low-symmetric rhombohedral GeTe crystals using high-angle annular dark-field scanning transmission electron microscopy (HAADF-STEM), Raman spectroscopy, and first-principles calculations. By analyzing the vibrational modes *via* the polarization- and temperature-dependent Raman results under parallel and cross configurations, we observed up to four Raman active modes. Based on this, the crystal orientation could be determined and the symmetry of the crystal structure could be understood. Furthermore, a strong four-phonon coupling process was analyzed during the change in temperature and

Key Laboratory of Polar Materials and Devices (MOE), Department of Electronics, East China Normal University, Shanghai 200241, China.
E-mail: fyyue@ee.ecnu.edu.cn, rjqi@ee.ecnu.edu.cn

† Electronic supplementary information (ESI) available. See DOI: https://doi.org/10.1039/d3nr02678g

the temperature-induced phase transitions between the α, γ, and β phases could be determined in GeTe.

2. Experimental and theoretical details

Single-crystalline rhombohedral (R) GeTe (α-phase) was purchased from 2D semiconductors. GeTe crystal with a thickness of less than ~5 mm was used in this work. Crystal X-ray diffractions (XRD) were performed at 300 K (Bruker D8 VENTURE) using Mo-Kα radiation (λ = 0.711 Å). Integration and scaling of intensity data were performed using the SAINT program. Data were corrected for the effects of absorption using SADABS. The cross-sectional TEM lamellae were fabricated on a dual-beam focused ion beam system (Helios G4 UX, FEI, USA) using Ga-ion accelerating voltages ranging from 2 to 30 kV. The (HAADF-STEM) images were acquired on a Cs-TEM (JEOL Grand ARM300) by an annular dark-field image detector with the inner semi-angle larger than 64 mrad. Raman measurements were performed on the inVia Reflex confocal micro-Raman spectrometer (Renishaw) equipped with a 532 nm excitation source from a solid-state laser and a 50× objective. For the polarization-dependent Raman measurement, a linear polarizer (or together with a waveplate) was placed before the detector to achieve parallel or cross configurations between the scattering and incident lights. During measurements, the sample was rotated with a step of 15°.

The electronic structure of bulk GeTe was calculated using the Kohn–Sham density functional theory (KS-DFT).[31] The real space electronic structure calculator (RESCU) was used to calculate the phonon modes and the phonon scattering relationship for bulk GeTe.[32,33] The exchange–correlation potential was described by the generalized gradient approximation (GGA) of the Perdew–Burke–Ernzerhof functional (PBE).[34] The Monkhorst–Pack scheme with 7 × 7 × 7 mesh was used to sample *k*-points of the Brillouin zone of bulk GeTe. The physical quantities were expanded using the real space lattice method, and the self-consistent field procedure was performed until the global charge variation was less than 10^{-5}. Lattice-dynamical properties were obtained for the Γ-point using the direct-force constant approach.

3. Results and discussion

Bulk α-GeTe belongs to a trigonal *R*3*m* space group, consisting of three Ge and three Te atoms in the unit cell. Ge^{2+} (Te^{2-}) is bonded to six equivalent Te^{2-} (Ge^{2+}) atoms to form a mixture of edge and corner-sharing $GeTe_6$ ($TeGe_6$) octahedra. The corner-sharing octahedral tilt angles are 10°. There are three shorter (2.86 Å) and three longer (3.25 Å) Ge–Te bonds. Fig. 1b and e show the representative HAADF-STEM images and the corresponding FFT patterns taken along $[\bar{1}00]_R$ and $[120]_R$ zone axes; these show the regular atomic arrangements of the armchair (AC) and zigzag (ZZ) directions, which are in line with the simulated structure of α-GeTe (Fig. 1a and d). The crystal plane spacing of $(\bar{2}10)$ and (003) is 0.211 nm and 0.363 nm, respectively. The zoom-in HAADF images in Fig. 1c and f show clear atomic configurations for both the AC and ZZ directions for R-phase GeTe with brighter spots representing Te columns and smaller ones for Ge columns. To get accurate phase information by using the powder XRD technique, we ground GeTe crystal into powders, so that we could obtain all the related diffraction peaks. As shown in Fig. 1g, together with the standard card of PDF#89-2552, all diffraction peaks could be indexed to an R-phase structure of the GeTe crystal with lattice parameters $a = b$ = 4.230 Å and c = 10.889 Å, which is in agreement with previous reports.[11,35]

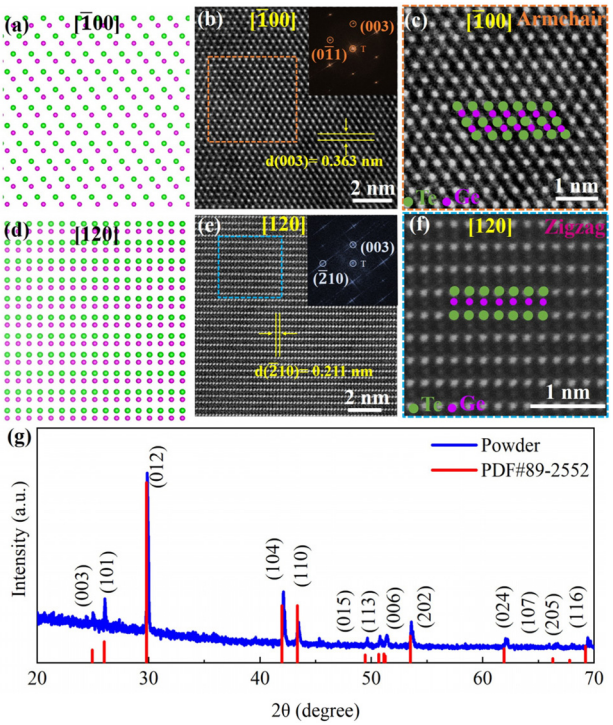

Fig. 1 (a) and (d) Simulated structure of α-GeTe along $[\bar{1}00]_R$ and $[120]_R$ zone axes. (b) and (e) The HAADF-STEM images of α-GeTe taken along $[\bar{1}00]_R$ and $[120]_R$ zone axes; the insets show the corresponding fast Fourier transform (FFT) patterns. (c) and (f) Zoomed-in images of the square regions in (b) and (e), respectively, for the corresponding AC and ZZ directions. (g) The powder XRD pattern of α-GeTe at room temperature.

We performed Raman measurements on the GeTe crystal at different temperatures. Fig. 2a shows the Raman spectra of bulk GeTe at 300 K and ~80 K (more details in Fig. S3†) with a similar curve shape. A fit procedure on the curve of 300 K roughly presented five peaks, which were denoted as A, B, C, D, and E at 88.1 cm^{-1}, 124.6 cm^{-1}, 142.2 cm^{-1}, 158.4 cm^{-1}, and 225.5 cm^{-1}, respectively. The two characteristic peaks, A and B, originated from the Ge–Te vibration; the former among these is the double-degenerate E symmetry transverse/longitudinal optical modes, and the latter is the A_1 symmetry transverse optical mode.[36–39] Peak C is due to the long-range inter-

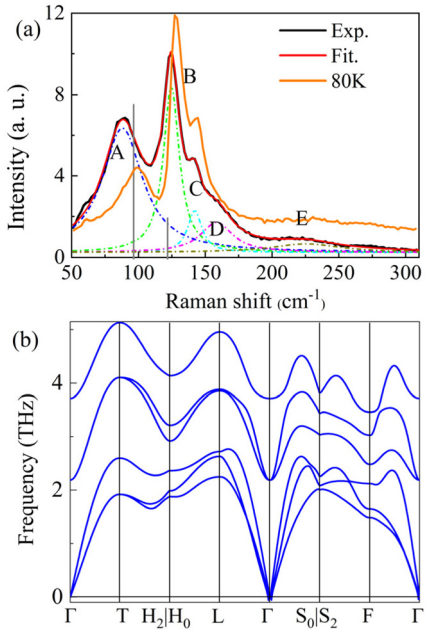

Fig. 2 (a) Raman spectrum of bulk GeTe at room temperature; solid curve – experimental result (red); vertical lines – calculated values (black). (b) The calculated phonon dispersion relations of bulk GeTe.

actions between crystalline Te, and peak D is triggered by the vibrational density of states of the long Te chains in disorder.[37,40] Peak E may be assigned to the antisymmetric stretching mode of the $GeTe_4$ tetrahedra.[41] The calculated Raman peaks by the density functional perturbation theory (DFPT)[42] are also shown with black vertical lines in Fig. 2a. Fig. 2b depicts the calculated phonon dispersion results. There are three acoustic waves with zero frequency at the Γ point, and the rest are optical waves. The phonon spectrum has negligible tiny virtual frequencies near the Γ point, indicating good dynamical stability of the model structure. Based on the group theory, GeTe has a total of two phonon modes, E (96.3 cm^{-1}) and A_1 (121.8 cm^{-1}), and both are Raman- and infrared-active. By comparing with the theoretical and experimental (at ~80 K) values in Fig. 2a, where the values of E and A_1 modes are experimentally 99 and 127 cm^{-1}, respectively, we can find a frequency difference in the two main modes, *i.e.*, ~2.7 and ~5.2 cm^{-1} blue shifts of E and A_1 modes, respectively. Inconsistency was also observed in low-symmetric $ReSe_2$,[43] whose reason was ascribed to the weak interlayer interaction due to the presence of both in-plane and out-of-plane components in their A_g vibrational modes. Therefore, the frequency shift in the A_1 mode may be understood as a competition between the interlayer coupling and the dielectric shielding. However, the maximum frequency shift of only 4 cm^{-1} in $ReSe_2$ was significantly different from that observed with the E mode. This suggests that other potential influences may be involved here, *e.g.*, the effect of temperature.[44] Notice that according to the DFT calculation (Fig. S1†), the direct E_g transition for bulk GeTe is located at the L point (E_g = 0.71 eV), and a slightly larger E_g can be seen at the T point (0.88 eV). The highest valence band (VB) and the lowest conduction band (CB) are dominated by the 4p orbital of Ge and the 5p orbital of Te, respectively. These observations are consistent with previous work[28] and verify the reliability and accuracy of the calculated results.

Polarization-resolved Raman measurements were further performed. Fig. 3a–d show the polar plot of the Raman intensity for the two Raman modes, E (88.1 cm^{-1}) and A_1 (124.6 cm^{-1}). The results for other modes are shown in Fig. S2;† the Raman modes exhibit different degrees of anisotropy. The E mode exhibits strong anisotropy in both cross (Fig. 3a) and parallel (Fig. 3c) configurations with a period of 90°, but with an angular difference of ~45° for the intensity maximum and minimum values. The mode of A_1 exhibits a two-lobe shape only in the cross configuration (Fig. 3b) with a period of 180°. While the behavior in the parallel configuration exhibits an asymmetric case (Fig. 3d), the poles correspond to the same angles as in the cross configuration. One of the reasons for this phenomenon may be the non-normal incident of the laser onto the surface of GeTe.

To better understand the results of polarization-resolved Raman spectroscopy of GeTe, the second-order Raman tensor for the Raman mode is taken into account. According to the classical Placzek approximation,[45] the Raman intensity can be written as,

$$I \propto |e_i \cdot R \cdot e_s|^2 \quad (1)$$

where R is the second-order polarizability tensor of Raman mode, abbreviated as the Raman tensor; e_i and e_s are the unit polarization vectors of the incident and scattered light, respectively. As GeTe belongs to the hexagonal system, the form of the Raman tensor is shown in Table 1.

In the current geometrical configuration, e_i and e_s are in the x–z plane. Thus, the incident polarization angle of θ is set

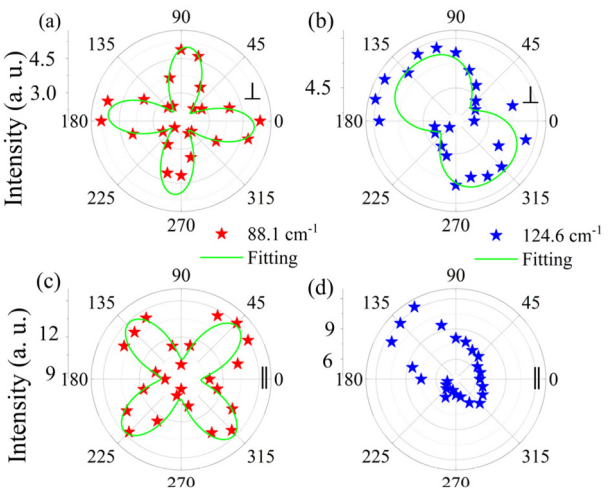

Fig. 3 (a)–(d) Polar plots of the peak intensity of E and A_1 modes under the polarization configurations (parallel or cross). Stars – experimental values; green curves – fit results.

Table 1 Raman tensors R for Raman-active modes in GeTe

Raman mode	E	A_1
R	$\begin{bmatrix} a & 0 & 0 \\ 0 & 0 & 0 \\ 0 & 0 & b \end{bmatrix}$	$\begin{bmatrix} c & 0 & 0 \\ 0 & -c & d \\ 0 & d & 0 \end{bmatrix}$

to the crystal axis, $e_i = (\cos\theta, 0, \sin\theta)$, while $e_s = (\cos\theta, 0, \sin\theta)^T$ (parallel polarization configuration) and $(-\sin\theta, 0, \cos\theta)^T$ (cross-polarization configuration). Table 2 shows the derived intensity for A_1 and E modes in parallel and cross-polarization configurations obtained from eqn (1). The measured data for E (88.1 cm^{-1}) mode exhibited a tetrad shape, which could be traced well by the equation listed in the table; also see Fig. 3a and c. However, the modes of 124.6 cm^{-1} (and 142.2 cm^{-1}) are poorly fitted, which may be due to the light absorption and birefringence effects mentioned above. There was no obvious rule for the 158.4 cm^{-1} mode, probably due to the vibration of disordered long Te chains. The period of 225.5 cm^{-1} in both configurations is 90°, which is the same as that of 88.1 cm^{-1} corresponding to the antisymmetric stretching mode of the $GeTe_4$ tetrahedron. Thus, for GeTe, the maxima of the E Raman intensity can be aligned along 0° in the parallel polarization configuration. This indicates that 0 or 90° corresponds to either the x- or y-axis of the GeTe crystal, indicating the crystal orientation.

Fig. 4a shows the Raman spectra of GeTe during the temperature range of 300–680 K (see Fig. S3† for results at low temperature). With the increase in temperature, the Raman peaks of the three strong modes showed different red-shifts and broadenings, which were generally related to anharmonic phonon interactions, electron–phonon coupling, or thermal expansion.[46] For clarity, Fig. 4b–d depict the temperature dependence of the peak intensity, position, and full-width at half-maximum (FWHM) of the three Raman modes. From Fig. 4b, we can see that the 88.1 cm^{-1} mode disappears beyond ~600 K, and the modes at 124.6 cm^{-1} and 142.2 cm^{-1} were not visible after 670 K; in addition, the clear inflection points (different slopes or disappearing) can be seen at 600 or 670 K (shadow zone), which may suggest that the GeTe undergoes different temperature-induced phase transitions. In Fig. 4c, all three modes were almost linearly red-shifted with an increase in temperature, which could be fitted with the following expression,

$$\omega(T) = \omega_0 + \chi T \quad (2)$$

where ω is the vibration frequency; ω_0 is the vibration frequency at 0 K; χ is the first-order temperature coefficient; and

Table 2 Raman scattering efficiency of E and A_1 modes in GeTe

E		A_1	
Parallel	Cross	Parallel	Cross
$(a\cos^2\theta + b\sin^2\theta)^2$	$\frac{1}{4}(b-a)^2\sin^2 2\theta$	$\lvert c\rvert^2\cos^4\theta$	$\lvert c\rvert^2\sin^2\theta\cos^2\theta$

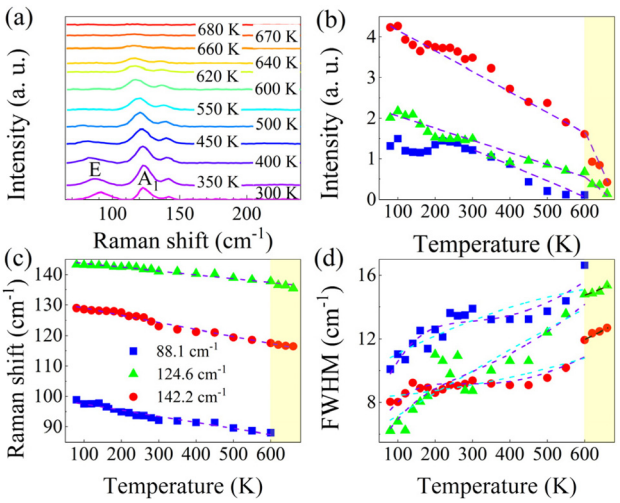

Fig. 4 (a) Raman spectra of GeTe at different temperatures. Temperature dependence of the peak intensity (b), position (c), and FWHM (d) of the three Raman modes, where the dashed lines represent the fit results or act as a guide for the eyes.

T is the absolute temperature (K). The fit by eqn (2) gave χ (88.1 cm^{-1}) = −0.0168 cm^{-1} K^{-1}, χ (124.6 cm^{-1}) = −0.0186, and χ (142.2 cm^{-1}) = −0.0165. Notice that the χ-values of the three modes do not differ much, and are smaller than that of SnS (B_{3g}: −0.029 cm^{-1} K^{-1}, A_g: −0.023 cm^{-1} K^{-1})[47] and BP (A_g: 0.0283 cm^{-1} K^{-1}, B_{2g}: −0.0271 cm^{-1} K^{-1}) with the orthogonal crystal system.[48] For 2D materials, the χ-value has been reported to be related to the van der Waals (vdW) interaction between neighboring layers, and the small χ-value indicates a weak electron–phonon coupling.[49,50]

Simultaneously, as shown in Fig. 4d, the FWHM of three modes shows different trends with increasing temperature, where the FWHM of 88.1 and 124.6 cm^{-1} modes shows a similar temperature-dependent trend but with a slight decrease in the temperature range of 300–450 K. It is well known that the smaller the FWHM is, the more regular the crystal vibration is and the more stable the crystal structure is. On the contrary, after 450 K the FWHM increases significantly, and the crystal structure starts to become unstable; additionally, the E and A_1 modes start to present thermal-related broadening. The 142.2 cm^{-1} mode showed an approximately linear evolution with the temperature here, which is mainly due to the presence of the homopolar bonding of Te–Te, a trend that is prevalent in Te compounds, such as BiTe.[51] When the temperature reaches 600 K, the E mode at 88.1 cm^{-1} disappears, and the A_1 mode at 124.6 cm^{-1} maintains a slightly linear increase till the temperature is beyond 670 K, where the Raman pattern approaches a curve with a very low signal-to-noise ratio without the appearance of evident peaks. A comparison with the results of Raman intensity and shift shows that these behaviors are consistent with the three key parameters.

It has been reported that GeTe can spontaneously transit between the polar α-phase (rhombohedral, low-temperature

phase) and the β-phase (cubic, high-temperature phase) at the Curie temperature of ~625 K,[52] and the phase transition temperature of GeTe is highly influenced by its stoichiometric ratio. For instance, Rinaldi *et al.* found that the tendency of Te to detach from GeTe at high temperatures leads to a change in its stoichiometric ratio.[17] Therefore, we believe that the GeTe has started to undergo a phase change, when the temperature is close to ~600 K, and may complete the phase transition process after ~670 K by referring to the similar temperature-dependent way and the almost simultaneous disappearance of the modes of 124.6 and 142.2 cm^{-1}. Thus, by combining with the phase diagram involving the composition ratio-dependent phase transition dynamics of GeTe,[10] we suggest that in the temperature range of 600–670 K, the status of GeTe comprises mixed α, γ, and β phases, *i.e.*, first from α phase to γ phase and then to β phase with the increase in temperature. For the high-temperature stable β phase with a sodium chloride structure, the previous report gave a phase transition temperature of 670 K,[53] and a close phase transition temperature of 673 K was also reported.[10]

Notice that the FWHM broadening of the Raman peaks can be fitted with the higher-order phonon scattering model proposed by Balkanski *et al.*:[54]

$$\Gamma = A + B\left(1 + \frac{2}{e^{x} - 1}\right) + C\left[1 + \frac{3}{e^{y} - 1} + \frac{3}{(e^{y} - 1)^{2}}\right] \quad (3)$$

where $x = \frac{\hbar\omega_0}{2k_B T}$; $y = \hbar\omega_0/3k_B T$; k_B is the Boltzmann constant; and $\hbar\omega_0$ is the specific vibration energy of a mode at 0 K. The constant (A) is the FWHM change caused by the phonon confinement effect and non-uniform strain; the constants B and C are the effects of three-phonon and four-phonon processes on the FWHM, *i.e.*, the excited optical phonon by photons decaying into two or three phonons, respectively, due to the non-harmonic effect when the material absorbs a photon. The fit curves (cyan) are shown in Fig. 4d, and the fitted (below 600 K) results by eqn (3) are given in Table 3. It shows that the A-values are roughly the same order of magnitude, but the B- and C-values vary significantly for different peaks. The 124 and 142 cm^{-1} modes, where both B- and C-values are positive, indicate that both three-phonon and four-phonon processes have positive effects on the FWHM. However, in the 88 cm^{-1} mode, the B is positive, and the C is negative, suggesting the opposite effects of three-phonon and four-phonon processes on the FWHM. Surprisingly, although the C-value is extremely small, it is still non-negligible during the fit procedure, indicating the presence of a four-phonon coupling process in GeTe during the temperature change.

Due to the lack of well-fitted data using the higher-order phonon scattering model, for phase-change materials, the temperature dependence of the FWHM of Raman peaks can be investigated by the model proposed by F. Jebari *et al.*,[55]

$$\Gamma = A' + B'T + C' \exp\left(-\frac{E_a}{kT}\right) \quad (4)$$

where E_a is the activation energy corresponding to the mode associated with the disorder mechanism; k is the Boltzmann constant; and A', B', and C' are the fitting parameters. This equation is widely used in the study of phase-change materials.[56,57] As shown in the dashed line (purple) in Fig. 4d, the experimental evolutions of the three modes can be fitted well by the model, of which the 88.1 and 124.6 cm^{-1} modes behave similarly below 600 K, and the 124.6 and 142.2 cm^{-1} modes vary approximately linearly above 600 K. The parameters fitted with eqn (4) are given in Table 4. The E_a values for the three models were approximately 8 kJ mol^{-1} below 600 K. By comparing the results of both models, we noticed that the higher-order phonon scattering model (eqn (3)) can still fit the evolution of the low-temperature range, indicating the existence of a four-phonon coupling in GeTe with increasing temperature. However, for the phase-change material, GeTe, eqn (4) is obviously more appropriate, where the linear part involving the A and B parameters represents the effect of vibrational relaxation, and the exponential term with the C parameter represents the GeTe crystal re-orientational relaxation.

Based on the FWHM of Raman peaks at different temperatures, we can semi-quantitatively estimate the thermal conductivity (K) of GeTe.[58]

$$K = \frac{1}{3} C_v \bar{V}^2 \tau_T \quad (5)$$

Where C_v, $\bar{V}$, and τ_T are heat capacity under constant volume, averaged acoustic phonon velocity, and the thermal transport relaxation time, respectively. Under the assumed conditions, where C_v is $2k_B$ and $\bar{V}$ is 5 km s^{-1},[4,59] the thermal transport relaxation time can be approximated as the quasi-particle lifetime of the Raman optical phonon τ, $\tau = \frac{1}{2\pi c\Gamma}$. By referring to the FWHM (Γ) value in the range of 8–16 cm^{-1}, τ ranges from 0.33–0.66 ps. The range of the K value from eqn (5) can then be 5.5–11.0 W m^{-1} K^{-1}, of which the mean value is ~8.25 W m^{-1} K^{-1}, which is extremely close to the previously-reported experimental value of 8.3 W m^{-1} K^{-1}.[60]

Table 3 Fitted data for the temperature-dependent FWHM results by eqn (3)

Raman shift (cm^{-1})	A (cm^{-1})	B (cm^{-1})	C (cm^{-1})
88 (E mode)	9.78	3.64×10^{-12}	-3.27×10^{-25}
124 (A_1 mode)	8.25	3.99×10^{-13}	1.87×10^{-25}
142 (Te–Te)	5.72	3.91×10^{-12}	5.06×10^{-25}

Table 4 Fitted data for the temperature-dependent FWHM results by eqn (4)

Parameters	88 (cm^{-1})	124 (cm^{-1})	142 (cm^{-1})
A'	6.41	5.14	3.79
B'	4.29×10^{-2}	3.01×10^{-2}	3.22×10^{-2}
C'	−44.45	−30.36	−22.81
E_a (kJ mol^{-1})	8.19	7.46	7.75

4. Conclusions

In summary, we present the first indication and interpretation of the vibrational modes of GeTe by combining observations with the experimental and theoretical Raman analysis; we provide an initial determination of in-plane anisotropy by polarization-resolved Raman spectroscopy, which can provide meaningful guidance to efficient thermoelectric studies due to the close relationship between structural anisotropy and the lattice thermal conductivity anisotropy. The crystal orientation of GeTe can be determined by the E mode; there is a strong four-phonon coupling process in the variable temperature process, which demonstrates a series of phase transitions starting at ~600 K and ending at ~670 K, which is close to previous reports. Based on the temperature-dependent FWHM of the Raman peaks, we can estimate not only the phase transition temperature and activation energy, but also the thermal parameters, including the thermal transport relaxation time and thermal conductivity. Our work may provide a useful guide to exploring the application of GeTe in thermoelectric, optoelectronic, and phase change memory devices.

Author contributions

F. Y. conceived this project. S. Y., F. S., and R. Q. prepared the samples. S. Y., F. S., R. Q., Y. L., S. D., and X. F. conducted the investigations and characterizations. F. Y. and R. Q. analyzed the data. S. Y. and F. Y. drafted the original manuscript. R. Q. and P. X. reviewed and edited the manuscript with contributions from all authors. We gratefully acknowledge HZWTECH for providing computation facilities.

Conflicts of interest

The authors declare that they have no competing interests.

Acknowledgements

This work is supported by the National Key Research Project (2022YFA1402902), the National Natural Science Foundation of China (12134003, 62274061, 61874043, 61790583), Shanghai Science and Technology Innovation Action Plan (21JC1402000).

References

1 F. Xia, H. Wang and Y. Jia, *Nat. Commun.*, 2014, **5**, 4458.
2 Z. Luo, J. Maassen, Y. Deng, Y. Du, R. P. Garrelts, M. S. Lundstrom, P. D. Ye and X. Xu, *Nat. Commun.*, 2015, **6**, 8572.
3 F. Sui, M. Jin, Y. Zhang, R. Qi, Y. N. Wu, R. Huang, F. Yue and J. Chu, *Nat. Commun.*, 2023, **14**, 36.
4 Y. Liu, S. Yang, F. Sui, R. Qi, S. Dong, P. Yang and F. Yue, *Phys. Chem. Chem. Phys.*, 2023, **25**, 3745–3751.
5 S. Huang, Y. Tatsumi, X. Ling, H. Guo, Z. Wang, G. Watson, A. A. Puretzky, D. B. Geohegan, J. Kong, J. Li, T. Yang, R. Saito and M. S. Dresselhaus, *ACS Nano*, 2016, **10**, 8964–8972.
6 X. Li, Y. Machida, A. Subedi, Z. Zhu, L. Li and K. Behnia, *Nat. Commun.*, 2023, **14**, 1027.
7 J. Wang, W. Liu and C. Wang, *Adv. Electron. Mater.*, 2023, **9**, 2201126.
8 Z. Zhou, T. Shen, P. Wang, Q. Guo, Q. Wang, C. Ma, K. Xin, K. Zhao, Y. Yu, B. Qin, Y. Y. Liu, J. Yang, H. Hong, K. Liu, C. Liu, H. X. Deng and Z. Wei, *Sci. Bull.*, 2023, **68**, 173–179.
9 A. Giussani, K. Perumal, M. Hanke, P. Rodenbach, H. Riechert and R. Calarco, *Phys. Status Solidi B*, 2012, **249**, 1939–1944.
10 H. Okamoto, *J. Phase Equilib.*, 2000, **21**, 496–496.
11 B. B. Jiang, W. Wang, S. X. Liu, Y. Wang, C. F. Wang, Y. N. Chen, L. Xie, M. Y. Huang and J. Q. He, *Science*, 2022, **377**, 208.
12 S. Perumal, S. Roychowdhury, D. S. Negi, R. Datta and K. Biswas, *Chem. Mater.*, 2015, **27**, 7171–7178.
13 S. Perumal, S. Roychowdhury and K. Biswas, *J. Mater. Chem. C*, 2016, **4**, 7520–7536.
14 M. Hong, Z. G. Chen, L. Yang, Y. C. Zou, M. S. Dargusch, H. Wang and J. Zou, *Adv. Mater.*, 2018, **30**, 1705942.
15 J. Li, X. Zhang, Z. Chen, S. Lin, W. Li, J. Shen, I. T. Witting, A. Faghaninia, Y. Chen, A. Jain, L. Chen, G. J. Snyder and Y. Pei, *Joule*, 2018, **2**, 976–987.
16 X. Y. Tan, J.-F. Dong, N. Jia, H.-X. Zhang, R. Ji, A. Suwardi, Z.-L. Li, Q. Zhu, J.-W. Xu and Q.-Y. Yan, *Rare Met.*, 2022, **41**, 3027–3034.
17 C. Rinaldi, S. Varotto, M. Asa, J. Slawinska, J. Fujii, G. Vinai, S. Cecchi, D. Di Sante, R. Calarco, I. Vobornik, G. Panaccione, S. Picozzi and R. Bertacco, *Nano Lett.*, 2018, **18**, 2751–2758.
18 Y. Yao, H. F. Huang, Y. J. Dong, H. Gu, J. L. Zhong, X. Hao and Y. Z. Wu, *Ann. Phys.*, 2022, **534**, 2100603.
19 S. W. Cho, Y. W. Lee, S. H. Kim, S. Han, I. Kim, J.-K. Park, J. Y. Kwak, J. Kim, Y. Jeong, G. W. Hwang, K. S. Lee, S. Park and S. Lee, *J. Alloys Compd.*, 2023, **957**, 170444.
20 D. Di Sante, P. Barone, R. Bertacco and S. Picozzi, *Adv. Mater.*, 2013, **25**, 509–513.
21 J. Krempaský, S. Muff, J. Minár, N. Pilet, M. Fanciulli, A. P. Weber, E. B. Guedes, M. Caputo, E. Müller, V. V. Volobuev, M. Gmitra, C. A. F. Vaz, V. Scagnoli, G. Springholz and J. H. Dil, *Phys. Rev. X*, 2018, **8**, 021067.
22 B. J. Kooi and J. Momand, *Phys. Status Solidi RRL*, 2019, **13**, 1800562.
23 P. Guo, A. Sarangan and I. Agha, *Appl. Sci.*, 2019, **9**, 530.
24 W. Zhang, R. Mazzarello, M. Wuttig and E. Ma, *Nat. Rev. Mater.*, 2019, **4**, 150–168.
25 K. Ren, M. Zhu, W. Song, S. Lv, M. Xia, Y. Wang, Y. Lu, Z. Ji and Z. Song, *Nanoscale*, 2019, **11**, 1595–1603.
26 J. Wang, L. Gao, S. Qu, H. Chen and J. Zhang, *Vacuum*, 2022, **200**, 111015.

27 S. Guo, Y. Wang, X. Zhang, B. Wang and J. Zhang, *Mater. Lett.*, 2022, **329**, 133199.
28 L. Vadkhiya, G. Arora, A. Rathor and B. L. Ahuja, *Radiat. Phys. Chem.*, 2011, **80**, 1316–1322.
29 A. Edwards, A. Pineda, P. Schultz, M. Martin, A. Thompson, H. Hjalmarson and C. Umrigar, *Phys. Rev. B: Condens. Matter Mater. Phys.*, 2006, **73**, 045210–045213.
30 Y. Zhao, L. Tang, S. Yang, K. Seng Teng and S. Ping Lau, *Opt. Lett.*, 2020, **45**, 1108–1111.
31 V. Michaud-Rioux, L. Zhang and H. Guo, *J. Comput. Phys.*, 2016, **307**, 593–613.
32 P. Kang, W.-T. Zhang, V. Michaud-Rioux, X.-H. Kong, C. Hu, G.-H. Yu and H. Guo, *Phys. Rev. B*, 2017, **96**, 195406–195408.
33 D. Liu, X. Chen, Y. Hu, T. Sun, Z. Song, Y. Zheng, Y. Cao, Z. Cai, M. Cao, L. Peng, Y. Huang, L. Du, W. Yang, G. Chen, D. Wei, A. T. S. Wee and D. Wei, *Nat. Commun.*, 2018, **9**, 193.
34 J. P. Perdew, A. Ruzsinszky, G. I. Csonka, O. A. Vydrov, G. E. Scuseria, L. A. Constantin, X. Zhou and K. Burke, *Phys. Rev. Lett.*, 2008, **100**, 136406.
35 D. Wu, L. D. Zhao, S. Hao, Q. Jiang, F. Zheng, J. W. Doak, H. Wu, H. Chi, Y. Gelbstein, C. Uher, C. Wolverton, M. Kanatzidis and J. He, *J. Am. Chem. Soc.*, 2014, **136**, 11412–11419.
36 M. J. Polking, J. J. Urban, D. J. Milliron, H. Zheng, E. Chan, M. A. Caldwell, S. Raoux, C. F. Kisielowski, J. W. Ager, R. Ramesh and A. P. Alivisatos, *Nano Lett.*, 2011, **11**, 1147–1152.
37 X. Zhang, F. Zhao, Y. Wang, X. Liang, Z. Zhang, Y. Feng, Y. Li, L. Tang and W. Feng, *ACS Appl. Mater. Interfaces*, 2020, **12**, 37108–37115.
38 D. Sarkar, G. Sanjeev and M. G. Mahesha, *Appl. Phys. A*, 2015, **119**, 49–54.
39 K. S. Andrikopoulos, S. N. Yannopoulos, A. V. Kolobov, P. Fons and J. Tominaga, *J. Phys. Chem. Solids*, 2007, **68**, 1074–1078.
40 R. De Bastiani, E. Carria, S. Gibilisco, M. G. Grimaldi, A. R. Pennisi, A. Gotti, A. Pirovano, R. Bez and E. Rimini, *Phys. Rev. B: Condens. Matter Mater. Phys.*, 2009, **80**, 245205–245206.
41 K. S. Andrikopoulos, S. N. Yannopoulos, G. A. Voyiatzis, A. V. Kolobov, M. Ribes and J. Tominaga, *J. Phys.: Condens. Matter*, 2006, **18**, 965–979.
42 S. Baroni, C. A. Dal, P. Giannozzi and G. S. De, *Rev. Mod. Phys.*, 2001, **73**, 515–562.
43 G. C. Resende, G. A. S. Ribeiro, O. J. Silveira, J. S. Lemos, D. Rhodes, L. Balicas, M. Terrones, M. S. C. Mazzoni, C. Fantini, B. R. Carvalho and M. A. Pimenta, *J. Raman Spectrosc.*, 2021, **52**, 2068–2080.
44 Y. El Mendili, B. Minisini, A. Abdelouas and J. F. Bardeau, *RSC Adv.*, 2014, **4**, 25827–25834.
45 R. Loudon, *Adv. Phys.*, 1964, **13**, 423–482.
46 S. Luo, X. Qi, H. Yao, X. Ren, Q. Chen and J. Zhong, *J. Phys. Chem. C*, 2017, **121**, 4674–4679.
47 J. Xia, X. Z. Li, X. Huang, N. Mao, D. D. Zhu, L. Wang, H. Xu and X. M. Meng, *Nanoscale*, 2016, **8**, 2063–2070.
48 A. Łapińska, A. Taube, J. Judek and M. Zdrojek, *J. Phys. Chem. C*, 2016, **120**, 5265–5270.
49 L. Pi, L. Li, X. Hu, S. Zhou, H. Li and T. Zhai, *Nanotechnology*, 2018, **29**, 505709.
50 X. Zhou, X. Hu, B. Jin, J. Yu, K. Liu, H. Li and T. Zhai, *Adv. Sci.*, 2018, **5**, 1800478.
51 P. Mal, G. Bera, G. R. Turpu, S. K. Srivastava, A. Gangan, B. Chakraborty, B. Das and P. Das, *Phys. Chem. Chem. Phys.*, 2019, **21**, 15030–15039.
52 M. J. Polking, M. G. Han, A. Yourdkhani, V. Petkov, C. F. Kisielowski, V. V. Volkov, Y. Zhu, G. Caruntu, A. P. Alivisatos and R. Ramesh, *Nat. Mater.*, 2012, **11**, 700–709.
53 G. S. Pawley, W. Cochran, R. A. Cowley and G. Dolling, *Phys. Rev. Lett.*, 1966, **17**, 753–755.
54 M. Balkanski, R. F. Wallis and E. Haro, *Phys. Rev. B: Condens. Matter Mater. Phys.*, 1983, **28**, 1928–1934.
55 F. Jebari, P. Becker and C. Carabatos-Nédelec, *J. Raman Spectrosc.*, 1994, **25**, 261–265.
56 M. Ben Gzaiel, A. Oueslati, J. Lhoste, M. Gargouri and A. Bulou, *J. Mol. Struct.*, 2015, **1089**, 153–160.
57 I. Gharbi, A. Oueslati, A. Bulou and M. Gargouri, *Mater. Res. Bull.*, 2021, **139**, 111250.
58 G. D. Mahan, *Condensed Matter in a Nutshell*, Princeton University Press, Princeton, 2011.
59 B. Marfoua, Y. S. Lim and J. Hong, *Phys. Chem. Chem. Phys.*, 2020, **22**, 12273–12280.
60 S. Perunnal, S. Roychowdhury, D. S. Negi, R. Datta and K. Biswas, *Chem. Mater.*, 2015, **27**, 7171–7178.